All-Dielectric Metasurfaces for Simultaneous Giant Circular Asymmetric Transmission and Wavefront Shaping Based on Asymmetric Photonic Spin–Orbit Interactions

*Fei Zhang, Mingbo Pu, Xiong Li, Ping Gao, Xiaoliang Ma, Jun Luo, Honglin Yu, and Xiangang Luo**

The control of polarization and wavefront plays an important role in many optical systems. In this work, a monolayer metasurface is proposed to simultaneously realize circular asymmetric transmission (AT) and wavefront shaping based on asymmetric spin–orbit interactions. Circularly polarized incidence, accompanied with arbitrary wavefront modulation, experiences spin-selected destructive or constructive interference. An extinction ratio of ≈10:1 and an AT parameter of ≈0.69 at 9.6 μm, as well as a full width half-maximum of ≈2.9 μm (≈30% of the peak wavelength), are measured with the designed metasurface. These measured results are more than four times of those achieved with previous monolayer chiral structures. As far as it is known, this is the first report on the realization of simultaneous giant AT and arbitrary wavefront modulation with only one metasurface. Due to its fabrication simplicity and the multifunctionality of the designed metasurface, this work may provide a promising route to replace bulky cascading optical components with only one ultrathin metasurface for chiroptical spectroscopy, chiral imaging, optical communication, and so forth.

1. Introduction

Simultaneous control of the polarization and wavefront of light is of critical importance to many light-based systems such as those for chiroptical spectroscopy and chiral imaging. Traditional methods for controlling the polarization and wavefront are complex combinations of linear polarizers, waveplates, and some phase retarders (such as prisms and lenses). These cascading optical components not only make the whole system bulky, thus far away from miniaturization and integration, but also reduce the efficiency and imaging quality. Recently, metasurfaces composed of a dense arrangement of resonant nanoantennas on a subwavelength scale have attracted increasing interests due to their extraordinary capability in the arbitrary control of electromagnetic waves.[1] Metasurface has thinner thickness, less energy losses, lower profile, and simpler fabrication process than those of bulky metamaterials.[2] One of the most important features is that metasurfaces allow considerable enhancement of photonic spin–orbit interactions (SOIs).[3] The SOIs describe the coupling between the spin and orbit degrees of freedom of photons during the transport of light.[4] Numerous exotic phenomena and fascinating flat optical devices based on SOIs in metasurfaces have been realized, including spin Hall effect,[5,6] imaging,[7,8] optical holograms,[9,10] vortex beam generators,[11,12] polarization converters,[13,14] among many others. Recently, metasurfaces have been reported to break the symmetry of photonic SOIs by merging Pancharatnam–Berry (PB) phase and waveguide retardation phase.[15,16] It means that the transmitted wavefronts with opposite spin states can be independently modulated, which opens new degrees of freedom for the photonic applications of SOIs and for the design of multifunctional metasurfaces.

In this work, we experimentally realized giant and broadband circular asymmetric transmission (AT), accompanied with wavefront manipulation for transmitted and reflected circularly polarized (CP) lights, based on our previous study of asymmetric SOIs.[15] AT (alternatively known as circular conversion dichroism) was observed in an anisotropic lossy planar chiral "fish-scale" structure by Fedotov et al. in 2006,[17] which is distinct from 3D continuous helical structures and stacked metallic structures.[18–20] The response of AT in some ways resembles Faraday rotation but requires no magnetic field or nonreciprocal materials for its observation. This property was utilized as optical diodes, circulators, and isolators for applications in chiroptical spectroscopy, ultrafast information processing, optical interconnects, communications, and so on.[17,21] Unfortunately, the chiral responses of monolayer chiral structures show narrow band and small AT parameter.[17,22–26]

Dr. F. Zhang, Prof. M. Pu, Prof. X. Li, P. Gao, Prof. X. Ma, Dr. J. Luo, Prof. X. Luo
State Key Laboratory of Optical Technologies on Nano-Fabrication and Micro-Engineering
Institute of Optics and Electronics
Chinese Academy of Sciences
Chengdu 610209, China
E-mail: lxg@ioe.ac.cn
Dr. F. Zhang, Prof. H. Yu
Key Laboratory of Optoelectronic Technology and System
Ministry of Education
Chongqing University
Chongqing 400030, China

DOI: 10.1002/adfm.201704295

The AT parameter is usually defined as the difference in total transmittance of CP light between forward and backward propagations.[27] 3D chiral metamaterials are expected to show higher performance,[21,28–32] but suffer from time-consuming optimization of structures as well as complex and difficult fabrication processes.[33]

Different from the approach of intrinsic chirality of antennas, the AT in our paper is achieved through the collective contribution from the array of supercells. Our approach avoids the complex design of intrinsic chiral antennas. The supercell is composed of two pairs of twin nanofins with different anisotropy and a relative rotation angle of $\pi/4$. The absence of the inversion symmetry of phase gradients of two converted spin components results in asymmetric SOIs. As a result, CP incidence undergoes spin-selective destructive or constructive interference, leading to the giant AT. The performance of our device is comparable to that of 3D chiral metamaterials and is achieved with only one step of lithography followed by a single etching process. Furthermore, PB phase can be introduced to manipulate the wavefront of transmitted and reflected CP lights while keeping good AT response. The realization of simultaneous giant AT and wavefront shaping with one metasurface can efficiently reduce the volume, weight, and cost of the optical systems for many applications. For instance, in a chiral imaging system, especially under the condition of low signal–noise ratio, our proposed metasurface could replace sophisticated setups requiring combinations of polarizers, waveplates, and lenses while reducing the disturbance from the noise (unwanted spin component).

2. Design of Wavefront Modulators with AT

2.1. Results and Discussion of AT

Figure 1a,b shows the schematic of a chiral supercell. The supercell is composed of two pairs of twin blue and green nanofins. Each nanofin is placed at the center of its corresponding subunit cell, whose period equals to the half of that of supercell. The green and blue nanofins have the same height but different sizes, as well as a rotation angle difference of $\alpha = \pi/4$. The designed patterns were fabricated through direct laser

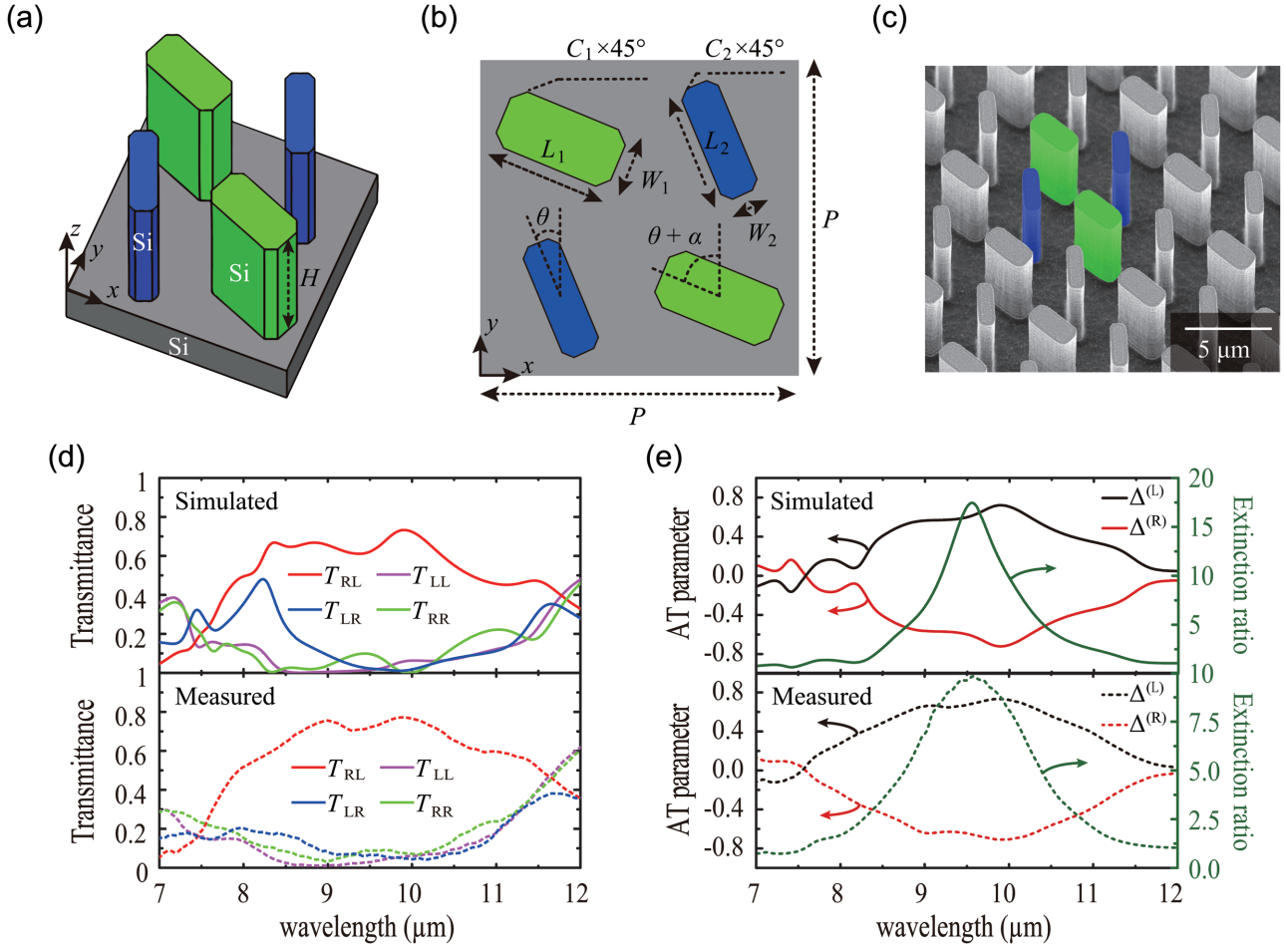

Figure 1. a) 3D and b) top views of all-silicon supercells showing the dimensions of $W_1 = 1.45$, $W_2 = 0.9$, $L_1 = 3.1$, $L_2 = 2.95$, $C_1 = 0.32$, $C_2 = 0.25$, $P = 8.1$, and $H = 6.0$ μm. c) SEM image of the fabricated metasurface. d) Jones matrixes of the metasurface with $\theta = \pi/8$. T_{RL} indicates RCP-transmission/LCP-incidence. Other elements (T_{LL}, T_{LR}, and T_{RR}) have similar definitions. e) AT parameters and extinction ratios of the metasurface. The measured transmittances were normalized to the Si wafer transmittance. Top (d and e): simulated results. Bottom (d and e): measured results.

writing in the resist on a double-sided polished silicon (Si) wafer (wafer thickness is ≈1.94 mm). Then an inductive-coupled plasmonic etching is subsequently employed to transfer the photoresist patterns into Si wafer to form the Si pillars. Figure 1c presents the scanning electron microscope (SEM) image of fabricated metasurface.

The metasurface was characterized with a Fourier-transform infrared spectrometer coupled with two linear polarizers and two superachromatic quarter wave plates (Bernhard Halle, phase error below ±1% within 1–15 μm). The characterization of the Jones matrix (T_{RL}, T_{LL}, T_{LR}, and T_{RR}) of the metasurface in circular polarization base is allowed by rotation of two linear polarizers. The simulated and measured Jones matrixes at normal incidence for forward propagation (+z direction) are in close agreement, as illustrated in Figure 1d. Both the measurements and simulations have shown giant and broadband AT. Note that there is a strong peak in the simulated T_{LR} curve at 8.3 μm that is very weak in the measurement. The reason for this discrepancy is clarified in the last paragraph in Section 2.2. Figure 1e displays the simulated and measured AT parameters and extinction ratios, which were characterized through the difference in and ratio of total transmittance of CP light between forward and backward propagations, respectively. $\Delta^{(R)}$ and $\Delta^{(L)}$ indicate the AT parameters for right and left handedness, respectively, and we chose left handedness during the characterization of extinction ratio. The measured results agree well with the simulated ones. Both peak wavelengths of AT parameters are around 9.9 μm, and both peaks of extinction ratios occur at 9.6 μm. We measured an extinction ratio of ≈10:1 and an AT parameter of ≈0.69 at the designed central wavelength of 9.6 μm, and the full width half-maximum (FWHM) of AT parameter is about 2.9 μm (≈30% of the peak wavelength). To the best of our knowledge, the maximum AT parameter of reported monolayer planar structures is about 0.15, and corresponding FWHM is about 3.5% of the peak wavelength (≈52.6 mm).[24] Our measured results are more than four times of those realized with monolayer planar structures and comparable to those achieved with 3D metamaterials. (Detailed data are presented in Table S1 in the Supporting Information.) In addition, our design is realized through simple fabrication processes. The simulated maximum extinction ratio is ≈17:1 at 9.6 μm, higher than the measured one. The discrepancy can be attributed to the scattering and nonnegligible material losses, as well as to the fabrication errors. Furthermore, multiple reflections inside the structured double-sided polished Si wafer, which do not exist in the simulation, may cause some discrepancy too.

2.2. Mechanism Analysis of AT

To present the physical mechanism of AT, we begin with the analyses of subunit cell. For simplicity, we assume every nanofin work as a local transparent half-wave plate that maximally converts CP incident light into transmitted light with opposite helicity. This can be realized via the proper design of the dimensions of nanofins. In this case, if a beam with arbitrary polarization $\mathbf{E}_i$ normally passes through metasurface from substrate, the resulting transmitted beams $\mathbf{E}_1$ and $\mathbf{E}_2$ for green and blue nanofins can be, respectively, written as[11,34]

$$\mathbf{E}_1 = \langle \mathbf{E}_i \,|\, R \rangle \exp(-\mathrm{i}2\theta - \mathrm{i}2\alpha - \mathrm{i}\phi) \,|\, L \rangle + \langle \mathbf{E}_i \,|\, L \rangle \exp(\mathrm{i}2\theta + \mathrm{i}2\alpha - \mathrm{i}\phi) \,|\, R \rangle \tag{1}$$

$$\mathbf{E}_2 = \langle \mathbf{E}_i \,|\, R \rangle \exp(-\mathrm{i}2\theta) \,|\, L \rangle + \langle \mathbf{E}_i \,|\, L \rangle \exp(\mathrm{i}2\theta) \,|\, R \rangle \tag{2}$$

where $|L\rangle = (0\ 1)^{\mathrm{T}}$ and $|R\rangle = (1\ 0)^{\mathrm{T}}$ denote left and right CP components (LCP and RCP, in circular basis), θ and $\theta + \alpha$ are the orientation angles of the two nanofins. The phase ϕ is the difference in waveguide retardation phase of cross-polarization between blue and green nanofins. The waveguide retardation phase is spin independent but related to the dimensions of antenna.[35] The phase ϕ plays an important role in asymmetric SOIs, which has been proved in our previous work.[15] A phase difference of $\phi = \pi/2$ is obtained at the central wavelength by suitably designing the dimensions of each nanofin. Simulated transmittances and phase shifts of blue and green nanofins are presented in **Figure 2**a,b. Thus, the overall phase difference of $\Delta\Psi$ between blue and green nanofins experienced by different spins of incidence for forward propagation is then

$$\Delta\psi = \phi + 2\sigma\alpha = \frac{\pi}{2} + \frac{\pi\sigma}{2} \tag{3}$$

where $\sigma = \pm 1$ denotes the spin state of CP incidence, which provides a phase difference of $\Delta\Psi = \pi$ for RCP → LCP, and $\Delta\Psi = 0$ for LCP → RCP. Thus, LCP incidence experiences constructive interference, therefore allowing full transmission of converted RCP, as shown in the top right of Figure 2c, while

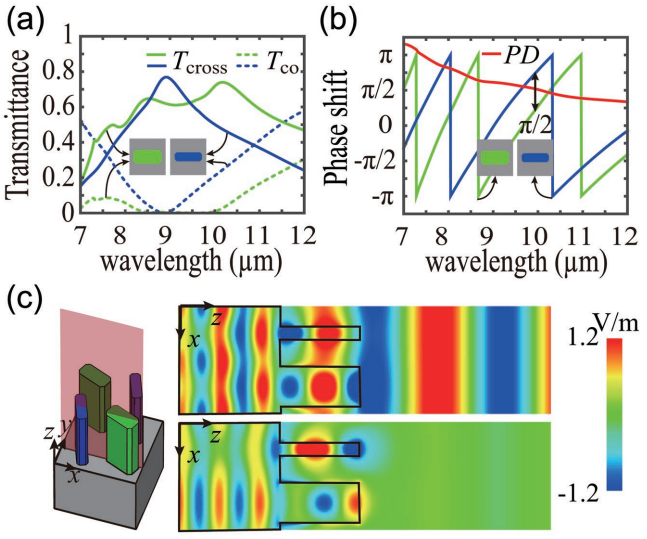

Figure 2. Simulated a) cross-polarization and copolarization transmittances and b) phase shifts of cross-polarization for two subunit cells as a function of wavelength. The results with LCP and RCP incidences are the same. The red curve in (b) indicates the phase difference in the phase shifts between two subunit cells. c) The distributions of electric field E_y in the periodic supercell (left) under the illumination of LCP (top right) and RCP (bottom right) light from the substrate side at the resonant wavelength of 9.9 μm.

RCP incidence undergoes destructive interference, leading to no converted LCP transmission and being reflected, as shown in the bottom right of Figure 2c. For backward propagation, the relative orientation angle between green and blue nanofins appears reversed when viewed from opposite sides, which means $\alpha = -\pi/4$. In this case, LCP incidence undergoes a phase difference of π and therefore is not transmitted (only reflected), while RCP incidence is converted into LCP transmission.

Figure 2a shows that there are four resonances in cross-polarized transmission (T_{cross}) curve of green nanofins at around 7.3, 7.7, 8.5, and 10.2 μm, but only one resonance at around 8.9 μm for blue nanofins. An abrupt phase shift usually occurs when these resonances are excited, which makes the phase difference in shorter wavelengths deviate more from $\pi/2$ than that in longer wavelengths, as illustrated in Figure 2b (red curve). Thus, a strong peak appears at around 8.3 μm in the simulated T_{LR} curve in Figure 1d. However, in reality, these resonances may be weakened due to nonperfection in fabrication processes, which makes the phase difference close to $\pi/2$ in short wavelengths. As a result, the measured T_{LR} and AT parameters are smoother than simulated ones at around 8.3 μm. Furthermore, the simulations of two subunit cells present that more than 20% of the energy is reflected due to impedance mismatch. If the demand for high efficiency is crucial, the AT parameter can be further improved by assigning different materials for nanofins and substrate. The gradient of refractive index can introduce a Fabry–Pérot cavity effect along the propagating direction, although at the cost of greater procedure complexity. For this more complex procedure, coating of Si and low-index films on Si substrate or coating of Si film on low-index substrate is required, but the fabrication processes are still simpler than those of 3D metamaterials.

2.3. Characterization of Wavefront Modulators with AT

The advantage of the design is that wavefront shaping with AT is accomplished through orientation-dependent PB phase factor $\exp(-i2\sigma\theta)$ in Equations (1) and (2) without any external lenses or spatial light modulators. Each nanofin can work as a weakly coupled low-quality-factor Fabry–Pérot resonator due to the high refractive index contrast between the nanofins and their surroundings,[36] in a similar way as the metalens based on metallic nanoslits array.[1] As a result, the metasurface will keep high performance of AT when changing the angle θ, as shown in **Figure 3**a. The phase shifts of RCP-transmission/LCP-incidence are presented in Figure 3b and show a good agreement with the PB phase of 2θ. Figure 3c illustrates that circular conversion dichroism also occurs in reflection spectrums. The phase shifts of LCP-reflection/RCP-incidence still agree well with PB phase in the working wavelength range, as shown in Figure 3d. It means that LCP (or RCP) incidence will produce diffraction patterns in reflection (or transmission) field.

To demonstrate the versatility and high performance of our proposed metasurface, we fabricated and characterized three typical flat wavefront modulators with high performance of AT. Figure 3e shows the schematic diagram of the modulation effects of these three modulators. The diffraction patterns of different colors represent the modulation effects of different modulators. Experimental results, optical microscope, and SEM images of the three devices are shown in **Figure 4**. Linearly polarized (LP) light at the wavelength of 9.6 μm was incident from the substrate to guarantee the energy of LCP and RCP portions to be equal.

The first device (deflector) was fabricated to demonstrate anomalous refraction and reflection that are different from the traditional PB-based metasurfaces. The traditional PB-based

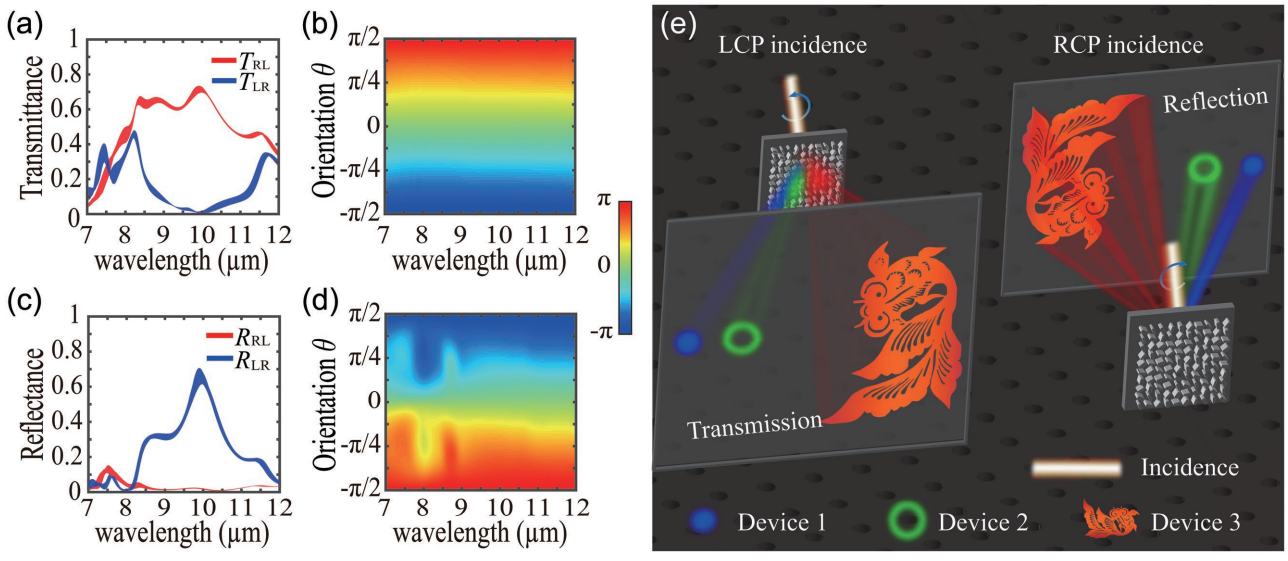

Figure 3. Simulated cross-polarized a) transmittances and c) reflectances of the supercell. Since the spectra differ depending on the orientation θ (ranging from $-\pi/2$ to $\pi/2$), they are plotted as a band in the graph. Simulated phase shifts of b) RCP transmission/LCP incidence and d) LCP reflection/RCP incidence as a function of the orientation θ and wavelength. e) The schematic illustration of the designed devices that generate diffraction patterns in the transmission (or reflection) field under the illumination of LCP (or RCP). Other diffraction orders with weak intensity are not shown in the schematic diagram.

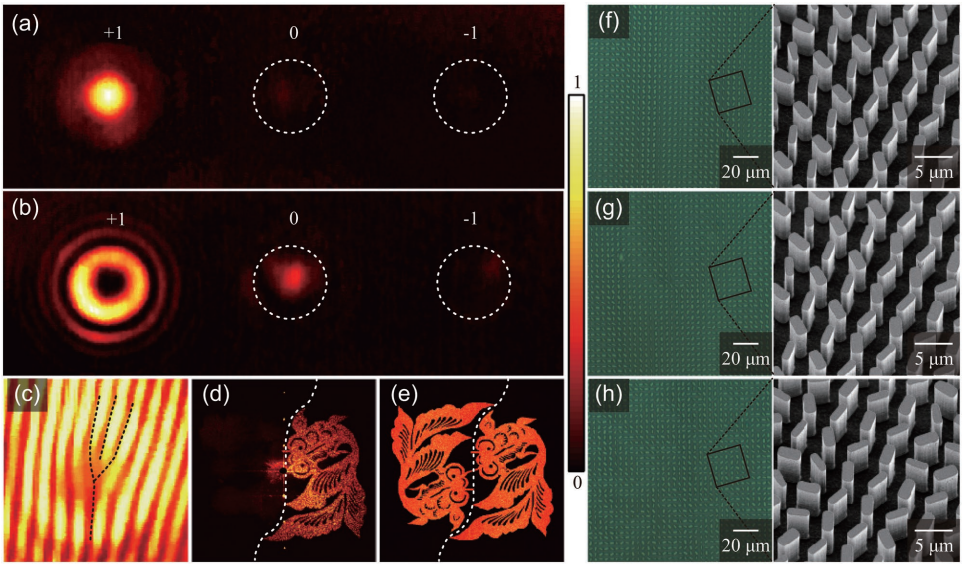

Figure 4. The measured results of three wavefront modulators with AT under the illumination of LP incidence. The transmitted diffraction patterns produced by the a) deflector and b) vortex generator. c) Interference patterns obtained through the interference of the vortex beam (produced with the vortex generator) and a titled Gaussian beam. d) The measured holographic images generated by the hologram. e) Theoretical holographic images created with traditional PB-based phase hologram. f–h) Optical microscope (left) and SEM (right) microscope images of the three wavefront modulators (from up to down: deflector, vortex generator, and hologram).The constant background produced by thermal radiation has been removed. White dashed curves in (d) and (e) are inserted to separate holographic images produced by the two spin components.

metasurfaces deflect both LCP and RCP portions of incidence in transmission or reflection field.[37,38] Our designed deflector separates LCP and RCP portions of incidence in transmission and reflection fields with opposite directions, respectively, as displayed in Figure 3e (blue diffraction patterns). The deflector consists of periodic arrays of eight supercells with an incremental rotation angle of $\pi/8$. Figure 4a shows the measured transmitted diffraction patterns. The central dim spot (0th order) is from the original spin component of transmitted beam, while the side bright (+1st-order) and dim (−1st-order) spots come from the anomalous refraction of two converted spin components. We measured efficiencies of 67.4%, 10.8%, and 4.2% for the +1st-, 0th-, and −1st-order diffractions, respectively, which support a contrast ratio of ≈16:1. The efficiency was characterized through the ratio of the diffraction power to the half of LP incidence power and then normalized to the Si wafer transmittance. The contrast ratio is defined as the ratio between the energy of ±1st-order diffractions. Figure S1a in the Supporting Information presents the measured reflected diffraction patterns of ±1st orders. It is observed that the intensities of ±1st-order diffractions show high contrast as well. The measured contrast ratio is ≈1:11.

Optical vortex has important applications in quantum optics, detection of rotating objects and optical communications.[11,39,40] In our experiment, the second device was fabricated to create a pure vortex beam in transmission and reflection fields, respectively, under the illumination of an LP wave. Such a capability may further promote the miniaturization and integration of the optical systems. The vortex generator is obtained by superimposing an azimuthal phase dependence $\exp(il\phi)$ on the abovementioned deflector, where ϕ is the azimuthal angle and l is the topological charge. Thus, the two devices (deflector and vortex generator) have the same diffraction angle, although the angles are shown to be different in Figure 3e to make the diagram clearer. The measured transmitted and reflected diffraction patterns are illustrated in Figure 4b and Figure S1b (Supporting Information), respectively. Both transmitted and reflected diffraction patterns show high contrast between ±1st orders. The separated beams (+1st order in transmission field and −1st order in reflection field) present pure donut-shape patterns that feature the generated vortices. Also, the topological charge of $l = +2$ can be identified through a dislocated interference fringe, as shown in Figure 4c, when the transmitted vortex (+1st order) and Gaussian beams interfere with a small angle (the angle sets the fringes spacing). The efficiency was not measured accurately due to the energy dissipation of vortex beam and the limitation of diffraction angle.

The last device is a phase hologram that generates one holographic image of a goldfish in transmission and reflection fields, respectively, under the illumination of LP light. Figure 4d displays the measured transmission intensity patterns. There is only one goldfish in the transmission field, and another goldfish appears in the reflection field. For traditional PB-induced phase hologram, two central symmetric goldfishes will simultaneously appear in transmission or reflection field,[9] as illustrated in Figure 4e (obtained through theoretical calculation). Due to AT, LP light can be selected as the excitation of the hologram without the disturbance from conjugate image. Such performance may provide extra degrees of freedom to design holograms. It should be noted that the disturbance could also be avoided in the sections of far field with traditional PB-introduced phase hologram, but at the cost of reducing available field. The designed phase hologram was calculated using the iterative Fourier-transform algorithm.[41] All the measured holographic images (Figure 4e) were obtained via field stitching due to the limitation of the detection size of infrared charge-coupled

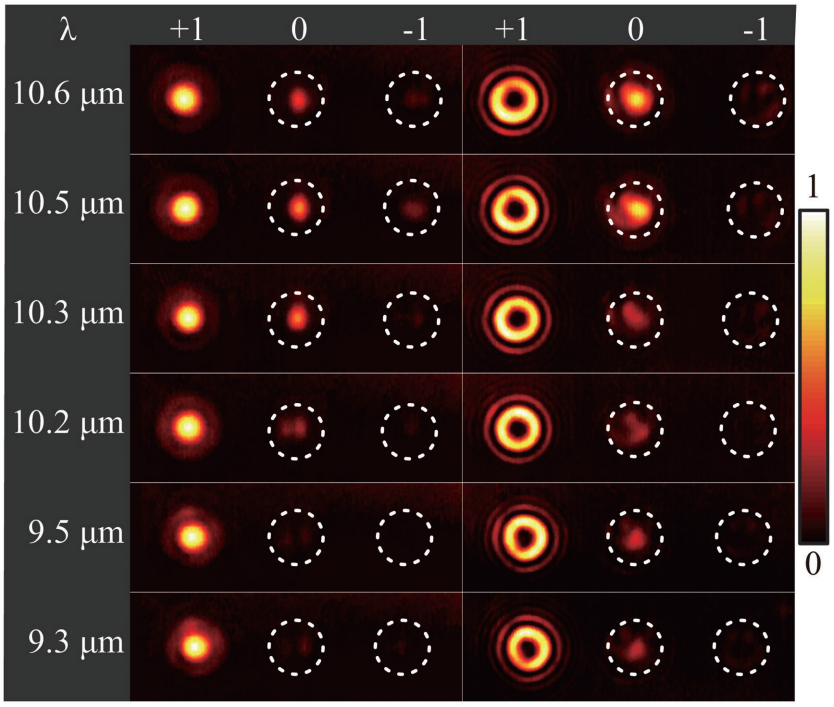

Figure 5. The measured diffraction patterns produced by the deflector (left) and vortex generator (right) at different wavelengths. The constant background produced by thermal radiation has been removed.

device (CCD). We avoided the zero-order light in the measurement in order to prevent the CCD from damage.

The broadband effect was characterized with the deflector and vortex generator under the illumination of LP light at several wavelengths ranging from 10.6 to 9.3 μm. **Figure 5** presents the measured transmitted diffraction patterns. It is obvious that the ±1st-order diffractions show high contrast in the whole range. The measured values of contrast ratios of the deflector at these wavelengths are about 11.1, 13.2, 15.1, 18.2, 15.5, and 13.7, respectively. The efficiencies are presented in Table S2 (Supporting Information). The efficiency of zero-order light increases with the increase of wavelength, which agrees well with the measured Jones matrix. The zero-order light of vortex generator is brighter than that of deflector mainly due to the energy dissipation of vortex beam, which reduces the intensity contrast between the +1st and 0th orders. Slight difference in the relative zero-order intensity between these two devices would be attributed to the fabrication errors.

3. Conclusion

In this article, we report asymmetric spin–orbit interactions that integrate circular AT and wavefront modulation into one monolayer all-silicon metasurface. The asymmetric spin–orbit optical phenomenon is achieved via merging PB phase and waveguide retardation phase.[15,35] We measured an extinction ratio of ≈10:1 and an AT parameter of ≈0.69 at a wavelength of 9.6 μm, as well as an FWHM of ≈2.9 μm. The performance is much better than that of previously reported monolayer chiral structures and comparable to that of 3D chiral metamaterials. The metasurface was obtained with only one step of lithography followed by a single etching process. Moreover, we demonstrated for the first time that AT and wavefront shaping can be simultaneously achieved through only one metasurface. Thus, one ultrathin metasurface could replace bulky optical setups requiring combinations of conventional components such as polarizers, waveplates, lenses, and spatial light modulators. This property enables considerable reduction of the volume, weight, cost, and energy loss of the optical systems. We believe that our work may have potential applications in the generation of complex optical fields and provide new ideas for studying chiral and functional materials.

4. Experimental Section

Simulation: The finite element method in CST Microwave Studio was employed to simulate the transmittances and phase shifts of the unit cells. The unit cell boundary conditions were applied at the *x* and *y* directions. For the *z* direction, the perfectly matched layer boundary was employed. The refractive index of Si was set as a constant of 3.36 according to the measured results displayed in Figure S2 (Supporting Information). High-order diffraction modes will appear in

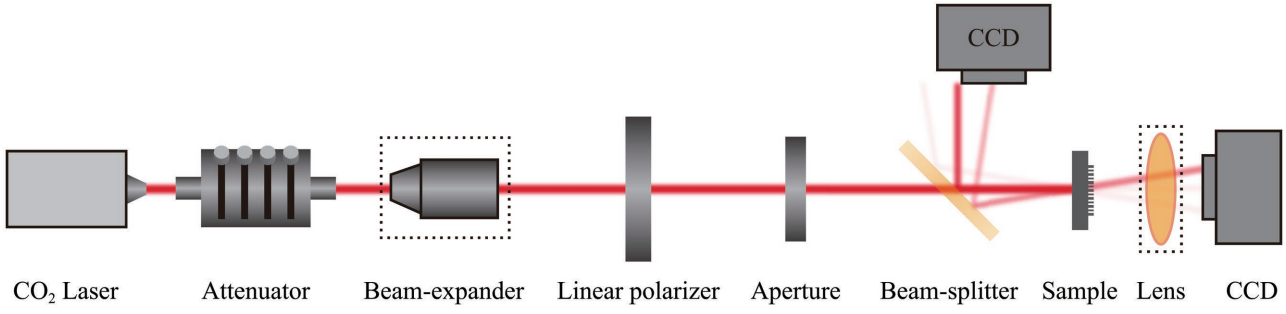

Figure 6. The schematic illustration of the measurement setup.

the substrate and reduce the efficiency, because the period of supercell does not satisfy the equivalent subwavelength condition ($P \leq \lambda/n$, where n is the refractive index of Si substrate) at $-z$ port. Thus, Floquet port with 98 modes was utilized at the $-z$ direction in simulations.

Measurement: **Figure 6** displays the schematic illustration of the measurement setup that was employed to characterize the designed wavefront modulators. The CO_2 laser was utilized as the light source. After passing through an adjustable attenuator, the optical beam was sent through a linear polarizer, followed by an adjustable aperture, and then transmitted to the sample from substrate. The transmitted diffraction patterns were recorded by an infrared CCD (384 × 288 pixels, UA330, Guide-Infrared Inc.). The size of each pixel was 25 μm × 25 μm. A beam splitter was utilized in front of the sample to guide the reflection to the infrared CCD. A beam expander and a lens were inserted into the setup during the measurement of holographic images. For the efficiency characterization, the infrared CCD was replaced with an infrared power meter.

Supporting Information

Supporting Information is available from the Wiley Online Library or from the author.

Acknowledgements

F.Z. and M.P. contributed equally to this work. This work was supported by the 973 Program of China (2013CBA01700) and the National Natural Science Funds (61622508, 61575201, and 61575032).

Conflict of Interest

The authors declare no conflict of interest.

Keywords

asymmetric transmission, metamaterials, metasurfaces

Received: July 29, 2017
Revised: August 28, 2017
Published online: October 23, 2017

[1] X. G. Luo, *Sci. China: Phys., Mech. Astron.* **2015**, *58*, 594201.
[2] M. Pu, X. Ma, X. Li, Y. Guo, X. Luo, *J. Mater. Chem. C* **2017**, *5*, 4361.
[3] M. Pu, Z. Zhao, Y. Wang, L. Xiong, X. Ma, C. Hu, C. Wang, H. Cheng, X. Luo, *Sci. Rep.* **2014**, *5*, 9822.
[4] V. S. Liberman, B. Y. Zel'Dovich, *Phys. Rev. A* **1992**, *46*, 5199.
[5] N. Shitrit, I. Bretner, Y. Gorodetski, V. Kleiner, E. Hasman, *Nano Lett.* **2011**, *11*, 2038.
[6] X. Luo, M. Pu, X. Li, X. Ma, *Light: Sci. Appl.* **2017**, *6*, e16276.
[7] M. Khorasaninejad, W. T. Chen, A. Y. Zhu, J. Oh, R. C. Devlin, D. Rousso, F. Capasso, *Nano Lett.* **2016**, *16*, 4595.
[8] M. Khorasaninejad, W. T. Chen, R. C. Devlin, J. Oh, A. Y. Zhu, F. Capasso, *Science* **2016**, *352*, 1190.
[9] D. Wen, F. Yue, G. Li, G. Zheng, K. Chan, S. Chen, M. Chen, K. F. Li, P. W. Wong, K. W. Cheah, *Nat. Commun.* **2015**, *6*, 8241.
[10] X. Li, L. Chen, Y. Li, X. Zhang, M. Pu, Z. Zhao, X. Ma, Y. Wang, M. Hong, X. Luo, *Sci. Adv.* **2016**, *2*, e1601102.
[11] M. Pu, X. Li, X. Ma, Y. Wang, Z. Zhao, C. Wang, C. Hu, P. Gao, C. Huang, H. Ren, *Sci. Adv.* **2015**, *1*, e1500396.
[12] J. Zeng, L. Li, X. Yang, J. Gao, *Nano Lett.* **2016**, *16*, 3101.
[13] X. Ding, F. Monticone, K. Zhang, L. Zhang, D. Gao, S. N. Burokur, L. A. De, Q. Wu, C. Qiu, A. Alù, *Adv. Mater.* **2015**, *27*, 1195.
[14] P. C. Wu, W.-Y. Tsai, W. T. Chen, Y.-W. Huang, T.-Y. Chen, J.-W. Chen, C. Y. Liao, C. H. Chu, G. Sun, D. P. Tsai, *Nano Lett.* **2016**, *17*, 445.
[15] F. Zhang, M. Pu, J. Luo, H. Yu, X. Luo, *Opto-Electron. Eng.* **2017**, *44*, 319.
[16] J. P. B. Mueller, N. A. Rubin, R. C. Devlin, B. Groever, F. Capasso, *Phys. Rev. Lett.* **2017**, *118*, 113901.
[17] V. A. Fedotov, P. L. Mladyonov, S. L. Prosvirnin, A. V. Rogacheva, Y. Chen, N. I. Zheludev, *Phys. Rev. Lett.* **2006**, *97*, 167401.
[18] J. K. Gansel, M. Thiel, M. S. Rill, M. Decker, K. Bade, V. Saile, F. G. Von, S. Linden, M. Wegener, *Science* **2009**, *325*, 1513.
[19] Y. Zhao, M. A. Belkin, A. Alù, *Nat. Commun.* **2012**, *3*, 870.
[20] J. Wu, B. Ng, H. Liang, M. B. H. Breese, M. Hong, S. A. Maier, H. O. Moser, O. Hess, *Phys. Rev. Appl.* **2014**, *2*, 014005.
[21] R. Ji, S. W. Wang, X. Liu, W. Lu, *Nanoscale* **2016**, *8*, 8189.
[22] V. A. Fedotov, A. S. Schwanecke, N. I. Zheludev, V. V. Khardikov, S. L. Prosvirnin, *Nano Lett.* **2007**, *7*, 1996.
[23] A. S. Schwanecke, V. A. Fedotov, V. V. Khardikov, S. L. Prosvirnin, Y. Chen, N. I. Zheludev, *Nano Lett.* **2008**, *8*, 2940.
[24] E. Plum, V. A. Fedotov, N. I. Zheludev, *Appl. Phys. Lett.* **2009**, *94*, 167401.
[25] R. Singh, E. Plum, C. Menzel, C. Rockstuhl, A. K. Azad, R. A. Cheville, F. Lederer, W. Zhang, N. I. Zheludev, *Phys. Rev. B* **2009**, *80*, 153104.
[26] C. Pan, M. Ren, Q. Li, S. Fan, *Appl. Phys. Lett.* **2014**, *104*, 167401.
[27] C. Menzel, C. Helgert, C. Rockstuhl, E. B. Kley, A. Tünnermann, T. Pertsch, F. Lederer, *Phys. Rev. Lett.* **2010**, *104*, 253902.
[28] L. Wu, Z. Yang, Y. Cheng, M. Zhao, *Appl. Phys. Lett.* **2013**, *103*, 2494.
[29] C. Pfeiffer, C. Zhang, V. Ray, L. J. Guo, A. Grbic, *Phys. Rev. Lett.* **2014**, *113*, 023902.
[30] W. Fan, Y. Wang, R. Zheng, D. Liu, J. Shi, *Opt. Express* **2015**, *23*, 19535.
[31] J. Kaschke, L. Blume, L. Wu, M. Thiel, K. Bade, Z. Yang, M. Wegener, *Adv. Opt. Mater.* **2015**, *3*, 1411.
[32] M. Kenney, S. Li, X. Zhang, X. Su, T. T. Kim, D. Wang, D. Wu, C. Ouyang, J. Han, W. Zhang, *Adv. Mater.* **2016**, *28*, 9567.
[33] M. Pu, C. Wang, Y. Wang, X. Luo, *Acta Phys. Sin.* **2017**, *66*, 144101.
[34] X. Chen, L. Huang, H. Mühlenbernd, G. Li, B. Bai, Q. Tan, G. Jin, C.-W. Qiu, S. Zhang, T. Zentgraf, *Nat. Commun.* **2012**, *3*, 1198.
[35] Y. Guo, M. Pu, Z. Zhao, Y. Wang, J. J. Jin, P. Gao, X. Li, X. Ma, X. Luo, *ACS Photonics* **2016**, *3*, 2022.
[36] F. Zhang, H. Yu, J. Fang, M. Zhang, S. Chen, J. Wang, A. He, J. Chen, *Opt. Express* **2016**, *24*, 6656.
[37] D. Lin, P. Fan, E. Hasman, M. L. Brongersma, *Science* **2014**, *345*, 298.
[38] A. Kildishev, A. Shaltout, J. Liu, V. Shalaev, *Optica* **2015**, *2*, 860.
[39] M. P. Lavery, F. C. Speirits, S. M. Barnett, M. J. Padgett, *Science* **2013**, *341*, 537.
[40] N. Bozinovic, Y. Yue, Y. Ren, M. Tur, P. Kristensen, H. Huang, A. E. Willner, S. Ramachandran, *Science* **2013**, *340*, 1545.
[41] R. W. Gerchberg, *Optik* **1971**, *35*, 237.

